



# Primary Support Design for Sequentially Excavated Tunnel Junctions in Strain-Softening Hoek–Brown Rock Mass

Vasileios I. Gkikas · Pavlos P. Nomikos

Received: 7 August 2020 / Accepted: 13 October 2020 / Published online: 28 October 2020  
© Springer Nature Switzerland AG 2020

**Abstract** Modern highway and railway tunnel projects include cross passages at regular intervals along the main tunnel length as escape routes. Such areas have complex geometry and incorporate three-dimensional stress redistributions in the tunnel support system and the rock mass. The sequential procedure of excavation and primary support installation of a tunnel junction area can be approximated only with complex three-dimensional numerical simulations. This study presents a practical methodology for the estimation of the displacements and loads induced to the main tunnel lining, after the construction of the escape tunnel. The methodology is based on the evaluation of three-dimensional numerical simulations results. All simulations incorporate sequential excavation and support cycles in confinement depended strain-softening Hoek–Brown rock mass. The results indicate that the area of the main tunnel lining in proximity to the crown of the escape tunnel is severely unloaded and tensile axial forces are possible to appear, while the main tunnel lining in proximity to the side walls of the escape tunnel is compressively overloaded. Finally, suitable support measures are proposed.

**Keywords** Tunnel junctions · Primary support · Strain softening rock mass · Hoek–Brown · Numerical modeling · FLAC3D

## 1 Introduction

Modern highway and railway tunnel projects include cross passages at regular intervals along the main tunnel length (rail or highway), as escape routes. The escape tunnels are for vehicles or passenger and the required intervals between each escape tunnel are specified according to the applicable design standards. Since it is common practice to construct twin tunnels, cross passages connecting them are commonly constructed to minimize the length of the escape tunnels. Such areas have complex geometry and incorporate three-dimensional stress redistributions to the support system of the tunnel and the rock mass. Considering that the sequential procedure of excavation and primary support installation of a tunnel is a complex three-dimensional problem itself, the tunnel junction area can be simulated only with complex numerical simulations.

The numerical simulation of the tunnel junction area requires the construction of a complex three-dimensional mesh and the sequential excavation and support in many calculation steps to provide realistic results. This simulation procedure is time consuming

---

V. I. Gkikas (✉) · P. P. Nomikos  
Tunnelling Laboratory, School of Mining and Metallurgical Engineering, National Technical University of Athens, 9 Iroon Polytechniou str,  
15780 Zografou, Athens, Greece  
e-mail: vasilis\_gikas@mail.ntua.gr

and it is usually avoided in design practice. The current study presents the results of three-dimensional numerical simulations of sequentially excavated tunnel junctions in various strain-softening Hoek–Brown rock masses. The results can be used in conjunction with plane strain numerical simulations to provide an approximation of the three-dimensional effects that take place in the junction area. However, since the true nature of each rock is much more complex than simply combining strength and deformability indices, it is strongly recommended to perform three dimensional simulations for the junction areas, especially in low quality rock masses or deep tunnels.

### 1.1 Background

The redistribution of stresses at the vicinity of the tunnel junction area is a complex three dimensional problem, and hence all recent research focus on three dimensional numerical simulations. Gerçek (1986) proposed several design and support considerations based on the results of previous studies such as Hocking (1978) and Brown and Hocking (1976). Guan et al. (1994) presented the results of 3D FEM simulations in comparison with field measurements. The work presented by Jones (2007) examines the junction area of a circular tunnel with a circular shaft with numerical methods in conjunction with field pressure cells measurements. Additionally, Hsiao et al. (2009) focused on the induced displacements to the roof of the main tunnel after the excavation of the escape tunnel for intersection angles 90°, 60° and 30° by performed elastic—perfectly plastic numerical simulations for various rock masses. Chen and Tseng (2010) presented a method to derive the 3D redistributed stress path into a 2D tunneling chart. Many authors (Bian et al. 2016; Gaspari et al. 2010; Li et al. 2016; Lin et al. 2013; Liu and Wang 2010) applied numerical methods in case studies and proposed design methods. Finally, Spyridis and Bergmeister (2015) investigated the lateral openings in the main tunnel lining, during breakout for the cross tunnel, for shallow circular tunnels in elastic soil.

### 1.2 Motivation

Although the simulation of the tunnel junction area has been the subject of previous research by many authors, a practical approach for a reliable and fast estimation

of the induced displacements, forces and moments to the main tunnel support system by the construction of the escape tunnel is not well established.

This study presents a practical methodology for the estimation of all the required quantities for the primary support design at the junction area based on the execution and interpretation of a large number of 3D numerical simulations. The three-dimensional finite differences code FLAC 3D (Itasca Consulting Group Inc. 2017) is used and the Hoek–Brown failure criterion is employed for both peak and residual rock mass strength. The transition from peak to residual strength follows a strain softening rule with confinement depended critical plastic strain. The post peak behavior of the rock mass is assumed to be brittle or abrupt strain softening for unconfined conditions with a gradual progression to ductile—perfectly plastic for a confining stress of the order of the rock mass uniaxial compressive strength  $\sigma_c$ , defined according to Hoek–Brown failure criterion (Hoek et al. 2002).

## 2 Tunnels, Rock Mass and Support

### 2.1 Geometry and Support Selection Criteria

The geometry of the tunnel excavation is derived from the geometry of the final lining with provision of an additional free space for the installation of the primary support and the waterproofing, construction tolerances, expected convergence of the surrounding rock mass and possible acceptable over-excavations. The cross sections of the examined tunnels are presented in Fig. 1 and represent the geometry of typical two-lane single branch tunnels and vehicle escape tunnels, respectively. In order to interpret and visually present the derived numerical results, longitudinal profiles are examined, along the main tunnel primary lining, which are defined according to the angle  $\theta$  ( $\theta = -90^\circ$  to  $+90^\circ$ ) at the cross section of Fig. 1a.

The excavation geometry introduced in the three-dimensional models was derived from these typical cross sections with an additional free space of the order of 20 cm. Although the actual excavation geometry varies for different primary support categories, the impact on the numerical results is considered negligible compared to the required effort to construct different 3D meshes for each support category.

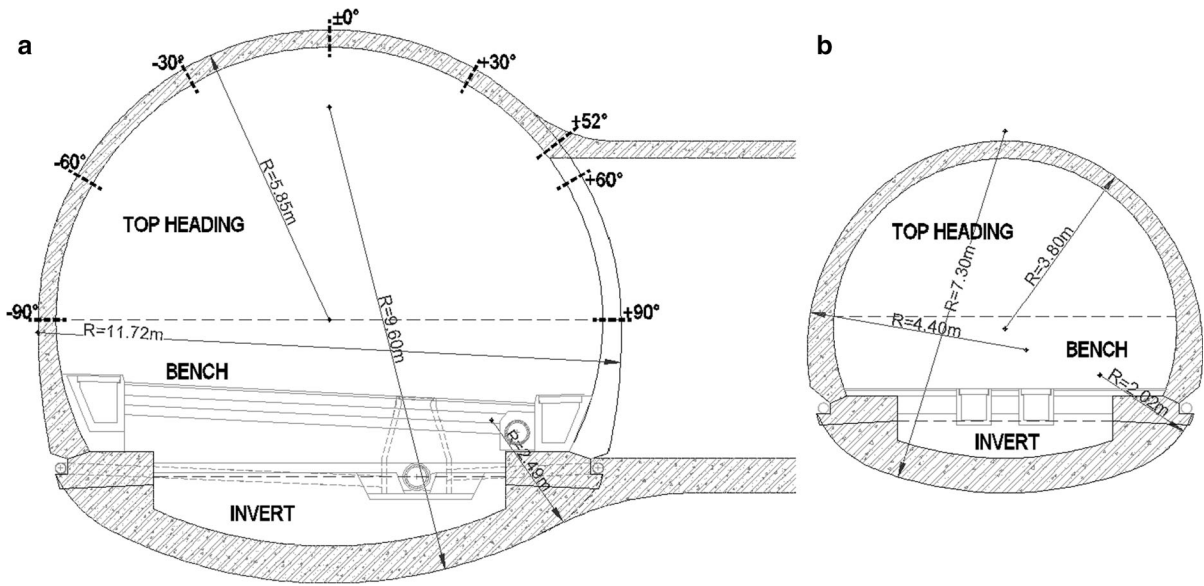


**Fig. 1** Typical cross sections of the examined tunnels: **a** main tunnel at the junction area, **b** vehicle escape tunnel

A crude support selection criterion was established in order to assign an appropriate primary support for each examined case based on the in-situ stresses and the rock mass strength and deformability. The criterion was based on the tunnel strain approach, presented by Hoek and Marinos (2000), which was adjusted for the current study according to the range of the anticipated strain levels estimated from a series of numerical simulations.

Primary support categories A, B, C and D, summarized in Table 1, were assigned to the two-lane tunnel for percent strain  $\epsilon = 0\text{--}0.1\%$ ,  $0.1\text{--}0.2\%$ ,  $0.2\text{--}0.3\%$  and  $> 0.3\%$  respectively. The primary support used for the vehicle escape tunnel was based on the support class of the two-lane tunnel. In cases were support classes A or B were selected for the main

tunnel, support class AB was applied at the vehicle escape tunnel, while for support type C and D for the main tunnel, support class CD was introduced for the vehicle tunnel. Since the contribution of the steel sets—lattice girders and of rock bolts on the stiffness of the support scheme is minor compared to its total stiffness, only shotcrete was considered in the numerical simulations, with a Young’s Modulus of 15 GPa and a Poisson’s ratio of 0.25.

The numerical simulation begins with the sequential excavation and support of the main tunnel top head in stages along its entire length, followed by the staged bench/invert excavation. After the excavation and support of the main tunnel, the primary support of the main tunnel at the junction area was removed (break-out) and the sequential excavation and support of the

**Table 1** Support categories used in the numerical simulations

Two-lane tunnel				Vehicle escape tunnel			
Support type	Allowable strain	Round length <sup>a</sup>	Shell thickness	Invert	Round length <sup>a</sup>	Shell thickness	Invert
PS-	$\epsilon$	$s$	$h$	×/✓	$s$	$t$	×/✓
A	< 0.1%	3 m/6 m	0.1 m	×	2 m/4 m	0.1 m	×
B	0.1–0.2%	2 m/4 m	0.2 m	×			
C	0.2–0.3%	1 m/2 m	0.3 m	×	1 m/2 m	0.25 m	✓
D	> 0.3%	1 m/2 m	0.4 m	✓			

<sup>a</sup>Top head/bench and invert

escape tunnel was simulated starting from inside the main tunnel towards the external boundaries of the model. The simulation procedure reflects the common practice in the majority of the construction of the escape tunnels and cross passages. In some cases, the escape tunnels are constructed prior to the main tunnel and used as intermediate access tunnels. Such special cases are not discussed in this paper and it is strongly recommended to perform three dimensional simulations due to the unique geometry of each case. It is noted that, in order to avoid overstressing of the primary lining of the main tunnel in extremely weak rock masses, the final lining of the main tunnel may be constructed before the escape tunnel is excavated. The specific design of the final lining is beyond the scope of the current research.

## 2.2 Rock Mass Quality and In Situ Stress Assumptions

The strength of the intact rock is a nonlinear function of its confinement. The Hoek–Brown failure criterion incorporates such behavior with plenty of experience gained from practical applications. In conjunction with the characterization of the rock mass with the geological strength index—*GSI* (Marinos et al. 2007), the generalized Hoek–Brown criterion (Hoek and Brown 2019) creates a practical and powerful tool for the description of the rock mass strength in engineering practice. In order to cover a wide range of rock masses, a range between 10 and 100 MPa was selected for the uniaxial compressive strength  $\sigma_{ci}$  of the intact rock. Each case of intact rock strength was paired with a typical intact rock Young's modulus  $E_i$ , a  $m_i$  value and a dilation angle  $\psi_i$  expressed as a function of the instantaneous equivalent friction angle  $\phi_i$  of the Mohr–Coulomb strength criterion which is evaluated during the numerical solution. It is noted here that the true nature of each rock is much more complex than simply combining strength and deformability indices. It is believed however that the selected  $\sigma_{ci}$  and  $E_i$  values cover common combinations that can be found in a wide variety of rocks (e.g. Deere and Miller 1966). The selected values of  $\sigma_{ci}$ ,  $E_i$ ,  $m_i$  and  $\psi_i$  are summarized in Table 2.

The fracturing of the rock mass was introduced with three *GSI* values, i.e.  $GSI = 30, 50$  and  $70$ , for each intact rock category. These values represent a disturbed, a very blocky and a blocky rock mass,

**Table 2** Selected values of the  $\sigma_{ci}$ ,  $E_i$ ,  $m_i$  and  $\psi$

$\sigma_{ci}$ (MPa)	$E_i$ (MPa)	$m_i$	$\psi_i/\phi_i$
10	10,000	10	0
25	20,000	12.5	1/16
50	30,000	15	1/8
75	45,000	17.5	1/6
100	60,000	20	1/4

respectively, commonly encountered in tunnels. Extremely high *GSI* values were not examined since the structure of such rock masses requires numerical techniques that explicitly simulate joints. Conversely, extremely low *GSI* values may lead to severe squeezing problems where the construction of a tunnel junction is not suggested or are unlikely to be found in intact rocks with high strength. No disturbance factor was introduced, reflecting the modern excavation and blasting techniques employed to minimize rock mass damage. In all the numerical models a hydrostatic natural stress field was considered for tunnel depths of 100 m, 300 m and 600 m within a rock mass with unit weight of 25 kN/m<sup>3</sup>.

## 3 Numerical Models

### 3.1 Simulation Approach

All the numerical simulations were carried out using the FLAC 3D finite differences code. In order to minimize the effect of the lateral boundaries a minimum distance of five tunnel diameters from each side of the main and escape tunnel was selected vertically and horizontally. The external dimensions of the 3D models were 90 m along the main tunnel axis, 130 m along the cross-tunnel axis and 130 m in the vertical direction. The actual geometry of the tunnels described was used to create the 3D mesh. All the lateral external boundaries were fixed in the normal direction (zero velocities perpendicular to the external boundary faces) while a normal stress was applied at the top of the model in order to initialize the primary stress field of each case. For the three depths examined and the combinations of rock masses used, only the models with values of  $\sigma/P_o$  between 0.2 and 1.3 were examined. Values below 0.2 were rejected in

order to avoid any squeezing problems and values above 1.3 due to practically elastic behavior of the rock mass. With the aforementioned limitations and assumptions, a total of 22 three-dimensional models were examined. Nine (9) models were with support class A, six (6) models with support class B, two (2) models with support class C and five (5) models with support class D. The number of top heading excavation and support stages varied from 30 to 90 depending on the support class. The number of bench–invert excavation and support stages were half of those of the top heading stages and varied between 15 and 45. In total approximately 1800 excavation and support stages were solved. An indicative view of the 3D model is presented in Fig. 2.

For the evaluation and interpretation of the results, longitudinal profiles of the deformations, axial forces and bending moments along the main tunnel lining were constructed, corresponding to different angles within the plane of the main tunnel as presented in Figs. 1a and 3. The profile at the crown of the main tunnel corresponds to an angle of 0°, while the base of the top heading is an angle ± 90° with intermediate profiles for angles ± 30° and ± 60°. Finally, a profile along the main tunnel that crosses the crown of the escape tunnel was constructed corresponding to an angle of + 52°. Along the escape tunnel, only one profile at its crown was constructed.

### 3.2 Constitutive Model

All the numerical simulations were carried out using the Hoek–Brown failure criterion (Hoek and Brown

2019). The peak strength envelope was estimated with the parameters presented in Table 2 for  $GSI = 30, 50$  and  $70$ . For the residual strength parameters, a reduction of the  $GSI$  value was introduced, as suggested by Cai et al. (2007), in order to represent the increased fracturing of the rock mass, where the strength of the intact rock is assumed to remain constant after the peak strength. Equation (1), proposed by Alejano et al. (2012) was used in this study for the estimation of the residual  $GSI_r$ .

$$GSI_r = 17.25e^{0.0107 \cdot GSI} \tag{1}$$

The rock mass deformation modulus was estimated with the parameters of Table 1 and the equation proposed by Hoek and Diederichs (2006). A confinement stress depended critical plastic shear strain was used in all the numerical models. The critical plastic shear strain is the strain level after which the material retains only its residual strength. The ratio of the drop modulus was estimated by using the methodology of Alejano et al. (2010) for unconfined conditions and by considering a softening branch of  $2G\eta$  as per Cundall et al. (2003). The  $\eta$  values for each peak  $GSI$  value are shown in Table 3.

The expression proposed by Cundall et al. (2003) was used for the estimation of critical plastic shear strain (Eq. 2), by using the peak values of Hoek–Brown strength parameters  $s$  and  $a$ , and by considering unconfined conditions ( $\sigma_3 = 0$ ):

$$\gamma_p^{cr}(\sigma_3 = 0) = \frac{\beta}{2G} \left( \frac{\eta + 1}{\eta} \right) \sigma_{ci} s^a \tag{2}$$

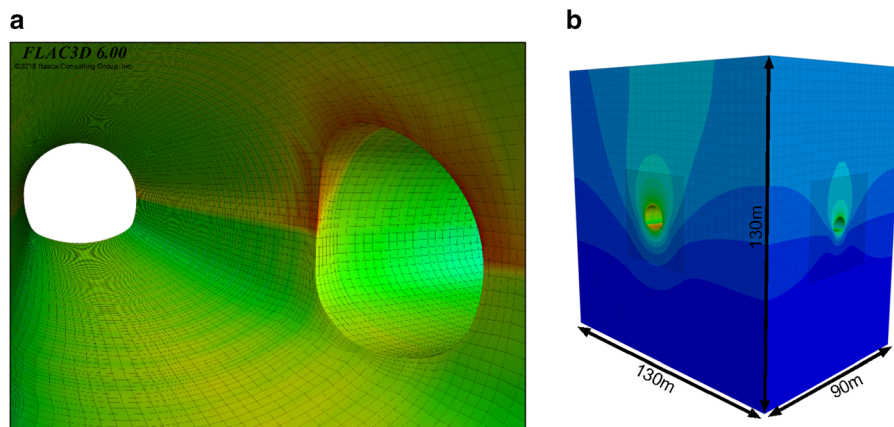


**Fig. 2** View and dimensions of the numerical models: **a** junction area, **b** external dimensions



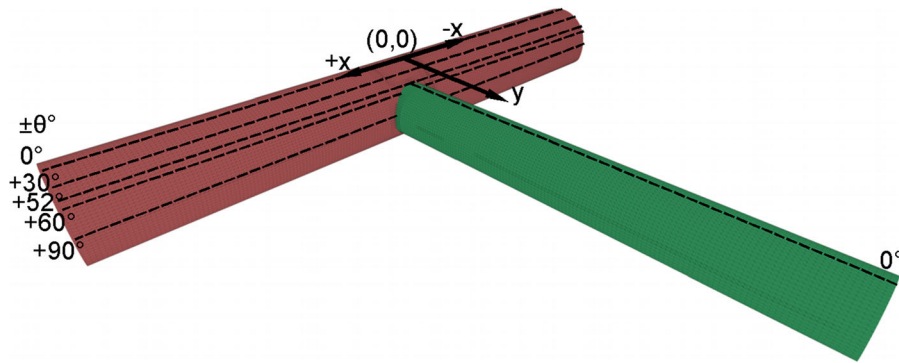


**Fig. 3** Positions of the critical longitudinal profiles evaluated

**Table 3** Softening branch  $\eta$  values for each peak  $GSI$  value

$GSI$	$\eta$
30	0.12
50	0.33
70	1.30

The parameter  $\beta$ , defined by Eq. (3), relates the peak and residual  $GSI$  values. Note that Cundall et al. (2003) proposed the use of parameter  $\beta$  in order to calculate a multiplier by  $(1 - \beta)$  for  $m_b$  and  $\sigma_{ci}$  so that the residual parameters are achieved. However, in this study, it is assumed that the residual parameters depend only on the additional fracturing introduced in the residual state.

$$\beta = 1 - \frac{GSI_r}{GSI} \tag{3}$$

The confinement stress dependency of the critical plastic shear strain was based on a multiplier ( $\mu$ ) of the latter according to Cundall et al. (2003) methodology, as presented with Eqs. (4) and (5). The multiplier was estimated in order to achieve the ductile behavior at the confinement level  $\sigma_3^{dc} = \sigma_c$ , where  $\sigma_c$  is the uniaxial compressive strength of the rock mass, defined according to the Hoek–Brown strength criterion (Hoek et al. 2002) as  $\sigma_c = \sigma_{ci} s^a$ .

$$\mu = \frac{\gamma_p^{cr}(\sigma_3)}{\gamma_p^{cr}(\sigma_3 = 0)} = \frac{\sigma_3^{dc}}{\sigma_3^{dc} - \sigma_3} = \frac{\sigma_c}{\sigma_c - \sigma_3}, \tag{4}$$

for  $\sigma_3 < \sigma_c$

$$\mu \rightarrow \infty, \text{ for } \sigma_3 \geq \sigma_c \tag{5}$$

To summarize the constitutive law used in the numerical models, the material initially behaves linearly in the elastic region deforming according to the rock mass Young’s modulus. After achieving its peak strength, as specified by the nonlinear generalized Hoek–Brown failure criterion with the peak  $GSI$  value, a softening branch is used for any further deformations. For very low confining levels the material behaves in a brittle manner. As the confinement increases, the critical plastic shear strain of the softening branch increases gradually according to the multiplier  $\mu$ . For elevated values of the confining stress, equal or greater than the uniaxial compressive strength of the rock mass, the slope of the softening branch is mild enough that approximates ductile behavior. At the critical plastic shear strain of each confining stress level the material constantly retains its residual strength for any further deformations, as specified by the nonlinear generalized Hoek–Brown failure criterion with the residual  $GSI_r$  values. A linear transition of the Hoek–Brown parameters at peak strength to the residual parameters at the critical plastic shear strain was assumed.

## 4 Results and Discussion

### 4.1 Displacements

#### 4.1.1 Main Tunnel

The diagram of Fig. 4a schematically presents the contour of the total displacements along the lining of a sequentially excavated and supported tunnel in stages (top head—bench/invert). The displacements vary

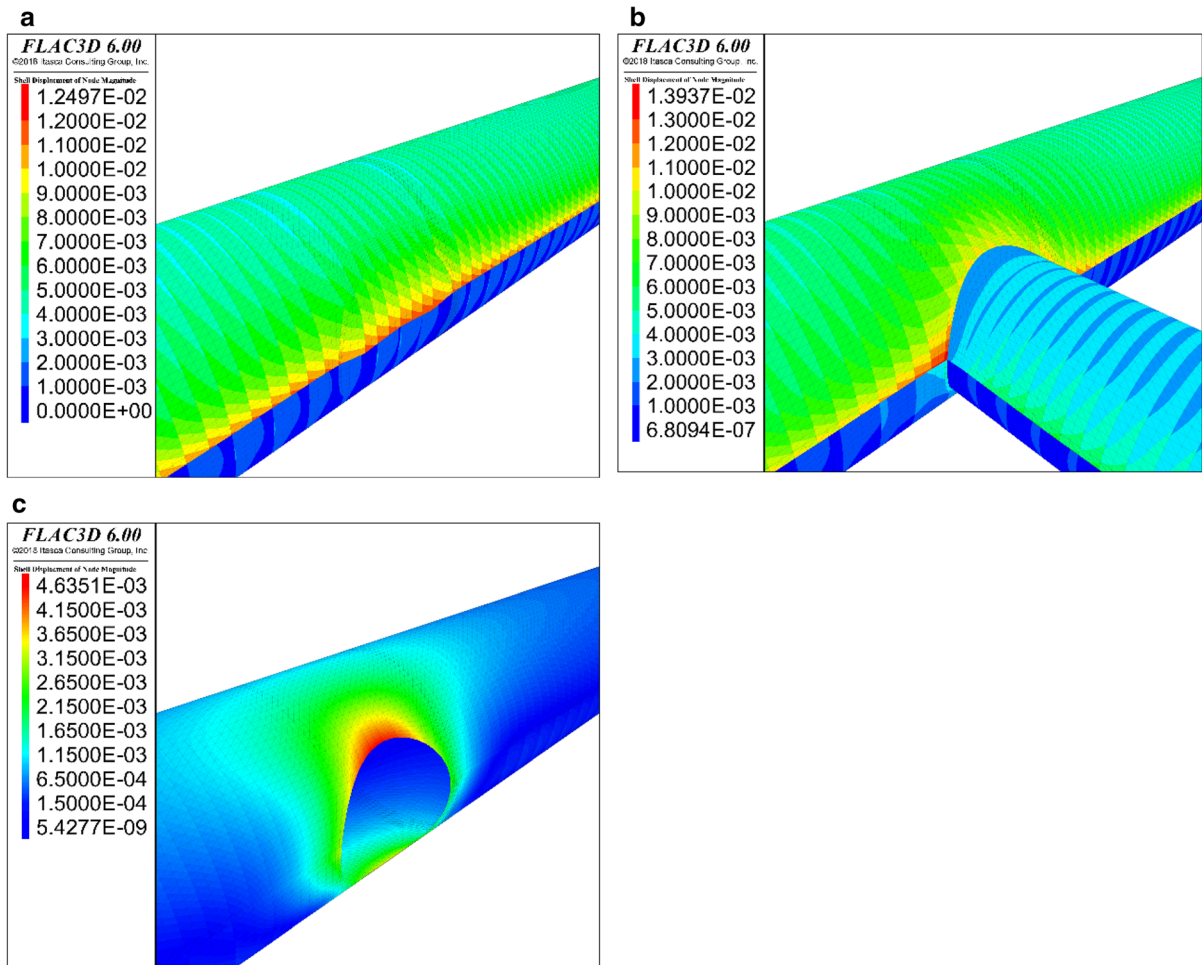


**Fig. 4** Displacement contours at the junction area: **a** total displacements prior to the construction of the escape tunnel, **b** total displacements after the construction of the escape tunnel,

**c** additional displacements of the main tunnel lining after the construction of the escape tunnel

along each excavation and support cycle due to the sequential construction, on both top head and bench/invert. After the breakout and the sequential excavation and support of the escape tunnel, the displacements of the existing main tunnel lining increase (Fig. 4b). The area that is severely affected is located at the junction with the crown of the escape tunnel. Due to the gradual removal of the escape tunnel core material, the rock mass converges towards the escape tunnel, drifting together the lining of the main tunnel which is rigidly connected to the rock mass. The additional displacements induced to the main tunnel lining due to the excavation and support of the escape tunnel are depicted in Fig. 4c.

Since the additional displacements of the main tunnel at the junction area  $\Delta u_{MT}$  are controlled by the excavation and support process of the escape tunnel, they are normalized with the total displacements of the cross tunnel  $u_{CT}(\infty)$  away from the junction area, as evaluated from the 3D numerical models. At the design stage,  $u_{CT}(\infty)$  may be estimated with the typical procedures used for the tunnel support dimensioning, such as plane strain numerical simulations. In case where 3D numerical simulations are used, an average value of the displacement along an excavation step should be used. The maximum normalized additional displacements, induced to the support of the main tunnel at the junction area after the

construction of the cross tunnel, are presented in Fig. 5a for all the different angles ( $-90^\circ$  to  $+90^\circ$ ) of the examined longitudinal profiles presented in Figs. 1 and 3. The additional displacements longitudinal profiles along the main tunnel lining, for angles that intersect the breakout area ( $\theta = 60^\circ$  and  $90^\circ$ ) are schematically represented in Fig. 6.

The distribution of the additional displacements along each longitudinal profile (for each angle  $\theta$ ) may be expressed with a Gaussian “bell curve” distribution:

$$\Delta u_{MT}(x) = \Delta u_{MT}(\xi) e^{-\frac{(x-\xi)^2}{2L_{MT}^u}} \tag{6}$$

where  $x$  is the lateral distance from the cross-tunnel centerline (located at  $x = 0$  as shown in Figs. 3 and 6),  $\Delta u_{MT}(x)$  the additional displacement at lateral distance  $x$ ,  $\Delta u_{MT}(\xi)$  the maximum additional displacement at the junction area appearing at a lateral distance  $x = \xi$  from the cross-tunnel centerline,  $L_{MT}^u$  the distance from  $x = \xi$  to the inflection point of the “bell curve”, which is referred to herein as the width of the distribution.

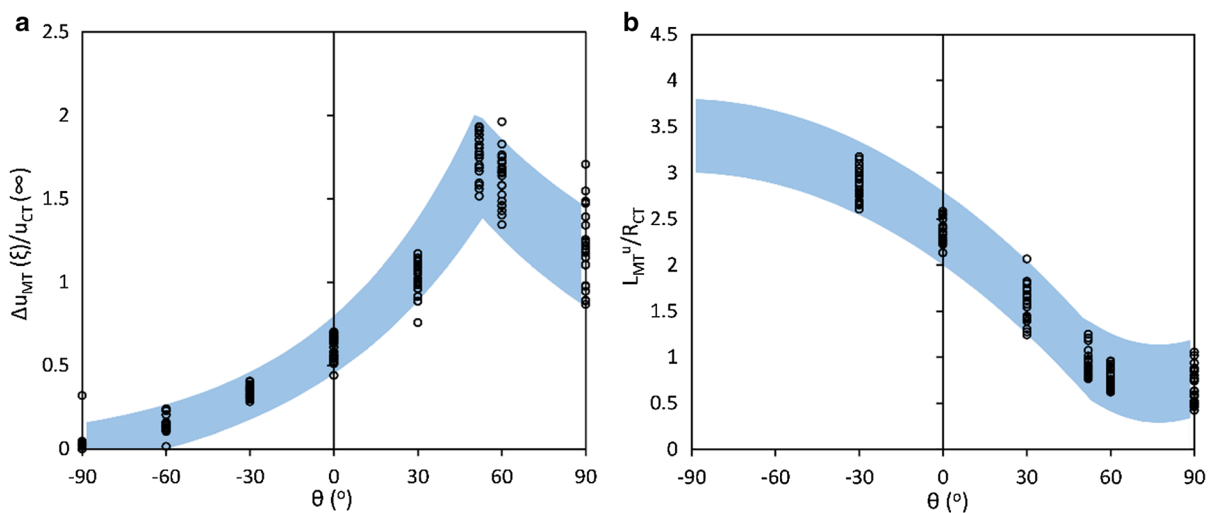
Figure 5a shows, the maximum additional displacement  $\Delta u_{MT}(\xi)$  for the various angles  $\theta$  of the examined profiles, normalized to the average crown displacement of the cross tunnel  $u_{CT}(\infty)$  away from the junction area. It is observed that the most adverse results are appearing for an angle  $\theta = 52^\circ$  which corresponds to the longitudinal profile tangent to the

cross-tunnel crown. Average values of the normalized maximum additional displacement  $\Delta u_{MT}(\xi)/u_{CT}(\infty)$  for each profile (i.e. for the various  $\theta$  values) may be obtained from column 2 of Table 4, while the position  $\xi$  of the maximum additional displacement may be obtained from column 3 of the same table.

The width  $L_{MT}^u$  of the additional displacements distribution, which practically defines the mostly affected area of the main tunnel lining due to the cross-tunnel excavation, is shown in Fig. 5b for the various angles  $\theta$  of the longitudinal profiles. For convenience,  $L_{MT}^u$  values in this diagram are normalized with the crown radius  $R_{CT}$  of the cross-tunnel. Average values of  $L_{MT}^u/R_{CT}$  may be obtained from column 4 of Table 4.

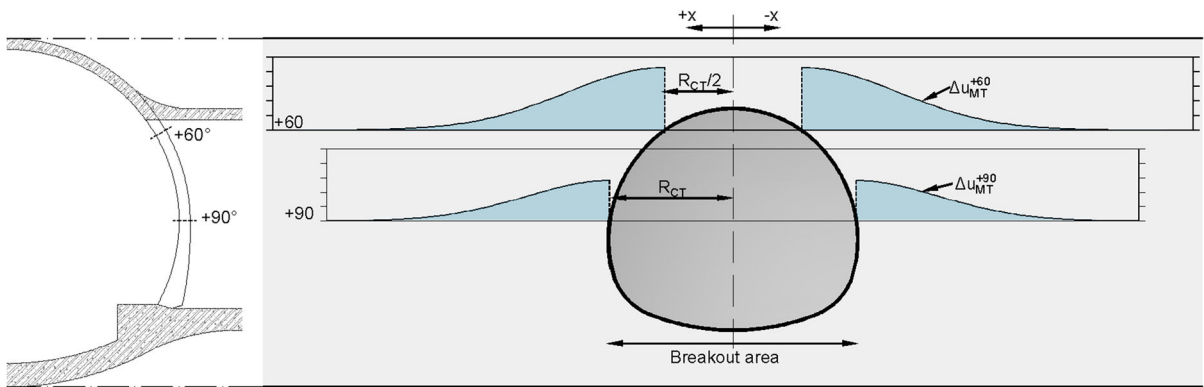
#### 4.1.2 Cross Tunnel

Figure 7 presents the displacements profile along the crown of a sequentially excavated and supported cross-tunnel in a rock mass with  $\sigma_c/P_o = 0.4$  and support class AB. Due to the sequential excavation and support, the displacements along each excavation step are not constant. Hence, an average displacement value for each excavation and support length along the cross-tunnel axis is used hereafter. Since the origin of the y-axis (parallel to the cross tunnel centerline) is at the main tunnel centerline, the cross tunnel excavation starts at  $y \approx 5$  m at the area of the cross-tunnel crown. Between that point and the first excavation face (at



**Fig. 5** a Maximum additional normalized displacements of the main tunnel lining after the construction of the escape tunnel for various angles  $\theta$ , b normalized width of the additional displacements distribution for various angles  $\theta$





**Fig. 6** Schematic representation of the additional displacements distribution for  $\theta = 60^\circ$  and  $\theta = 90^\circ$

**Table 4** Average values required in Eq. 6 for the estimation additional displacements along each longitudinal profile

$\theta$ ( $^\circ$ )	$\Delta u_{MT}(\xi)/u_{CT}(\infty)$	$\xi$	$L^u_{MT}/R_{CT}$
- 90	0.015	0	$\sim 3.3$
- 60	0.15	0	$\sim 3.2$
- 30	0.35	0	2.87
0	0.60	0	2.35
30	1.02	0	1.58
52	1.75	0	0.94
60	1.62	$\pm R_{CT}/2$	0.70
90	1.20	$\pm R_{CT}$	0.65

$y = d$ ), the cross-tunnel crown displacements gradually increase. For  $y > d$ , the cross-tunnel crown displacements gradually decrease and eventually become equal to the average value  $u_{CT}(\infty)$  away from the junction area. The maximum value of the cross-tunnel crown displacement at  $y = d$  can be estimated as the sum of  $u_{CT}(\infty)$  and an additional displacement  $\Delta u_{CT}(d)$  due to the proximity with the main tunnel. In Fig. 8a, the additional displacements  $\Delta u_{CT}(d)$ , as obtained from the 3D numerical simulations of the current study, are plotted for various  $\sigma_c/P_o$  values.

The drop rate of the additional cross-tunnel crown displacements is specified by the parameter  $L^u_{CT}$ . The

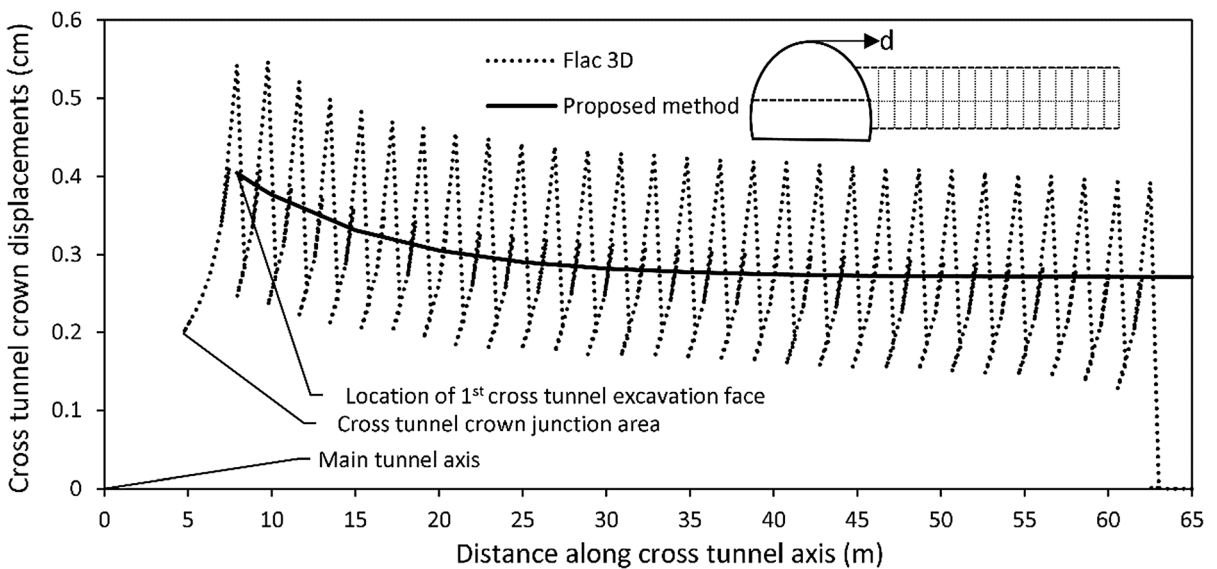


**Fig. 7** Displacements along the cross tunnel crown

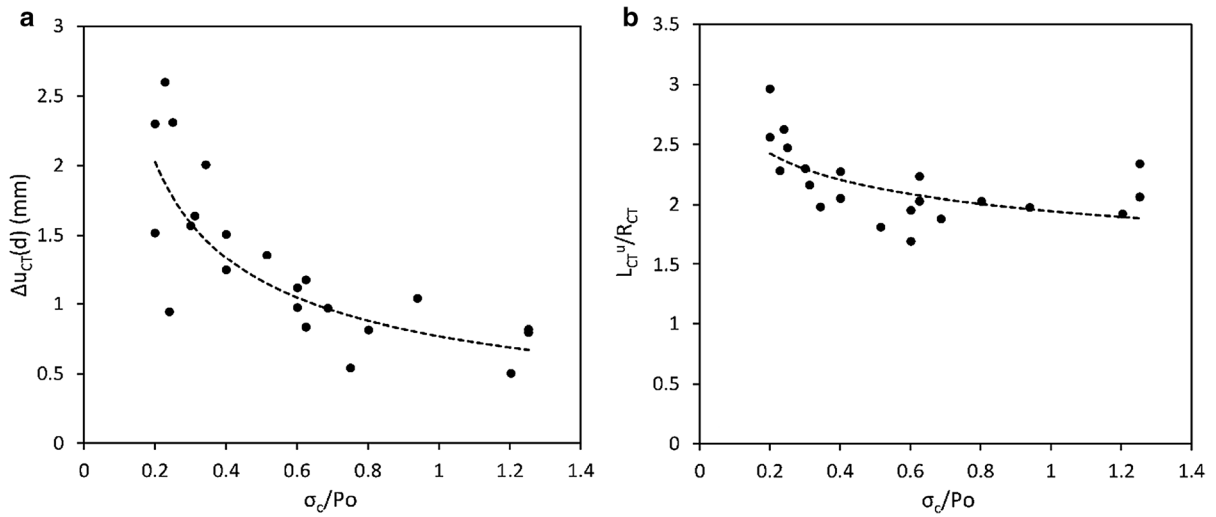


**Fig. 8** **a** Maximum additional cross-tunnel crown displacements, **b** width of the normalized cross-tunnel crown displacements profile

normalized value of  $L_{CT}^u$  with the cross tunnel crown radius  $R_{CT}$  can be estimated with Fig. 8b for various  $\sigma_c/P_o$  values.

The cross-tunnel crown displacements profile for  $y > d$  can then be plotted with Eq. 7.

$$u_{CT}(y) = \Delta u_{CT}(d)e^{-\frac{(y-d)}{L_{CT}^u}} + u_{CT}(\infty), y \geq d \quad (7)$$

where  $y$  is the lateral distance from the main-tunnel centerline (Figs. 3, 7),  $d$  the position of the first cross-tunnel excavation face (Fig. 7),  $\Delta u_{CT}(d)$  the additional crown displacement at  $y = d$  (which may be obtained from Fig. 8a),  $u_{CT}(\infty)$  the average crown displacement of the cross tunnel away from the junction area and  $L_{CT}^u$  the width of the cross tunnel crown displacements distribution (Fig. 8b).

#### 4.2 Membrane Action (Hoop Axial Forces)

The hoop axial forces along the lining of a sequentially excavated and supported tunnel in stages (top head—bench/invert) vary along each excavation and support cycle, both for top head and bench/invert excavation. After the breakout and the sequential excavation and support of the escape tunnel, the hoop axial forces of the existing main tunnel lining are severely affected in two discrete areas (Fig. 9). Area A of the main tunnel lining in proximity to the crown of the escape tunnel is severely unloaded and tensile axial forces are possible to appear in poor tunneling conditions. The additional displacements mechanism, described previously in

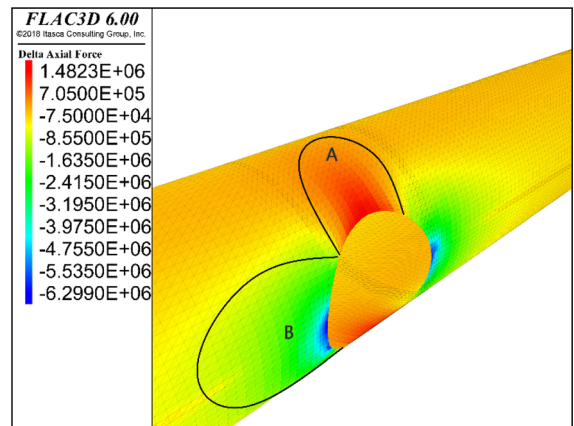


**Fig. 9** Change of hoop axial forces after the construction of the escape tunnel

Sect. 4.1, gradually unloads the compressive hoop axial forces, developed onto the lining of the main tunnel during its construction, making the development of tensile axial forces possible. Area B of the main tunnel lining in proximity to the wall of the escape tunnel is severely loaded. The tangential stresses that were developed within the rock mass due to the main tunnel construction, along with the additional stresses due to the escape tunnel, are arched towards the rock column at the side walls of the two tunnels and result in severe compressive stresses and plastic deformations. Those stresses result in the development of compressive hoop axial forces to the already installed lining of the main tunnel, but they do

not affect the lining of the cross-tunnel that is loaded from the excavation of the next cross-tunnel stage. The cross-tunnel lining axial forces are generally lower at the junction area in comparison to their respective values away from the junction area.

The maximum change of the hoop axial forces at the junction area  $\Delta N_{hoop}(\xi)$  [MN/m] is normalized with the shell thickness  $h$  for each support category A to D used in the various numerical models examined. The shell thickness ( $h$ ) values are presented in Table 1 for each support category. The results of the aforementioned normalization are presented in Fig. 10a for all the different angles ( $-90^\circ$  to  $+90^\circ$ ) of the longitudinal profiles examined and presented in Figs. 1 and 3.

Similarly to the additional displacements, the distribution of the change of the hoop axial forces  $\Delta N_{hoop}(x)$  [MN/m] along each longitudinal profile may be expressed with a Gaussian “bell curve” distribution with maximum value  $\Delta N_{hoop}(\xi)$ , acting at lateral distance  $x = \xi$ , and width  $L_{MT}^N$ .

$$\Delta N_{hoop}(x) = \Delta N_{hoop}(\xi) e^{-\frac{(x-\xi)^2}{2L_{MT}^N}} \tag{8}$$

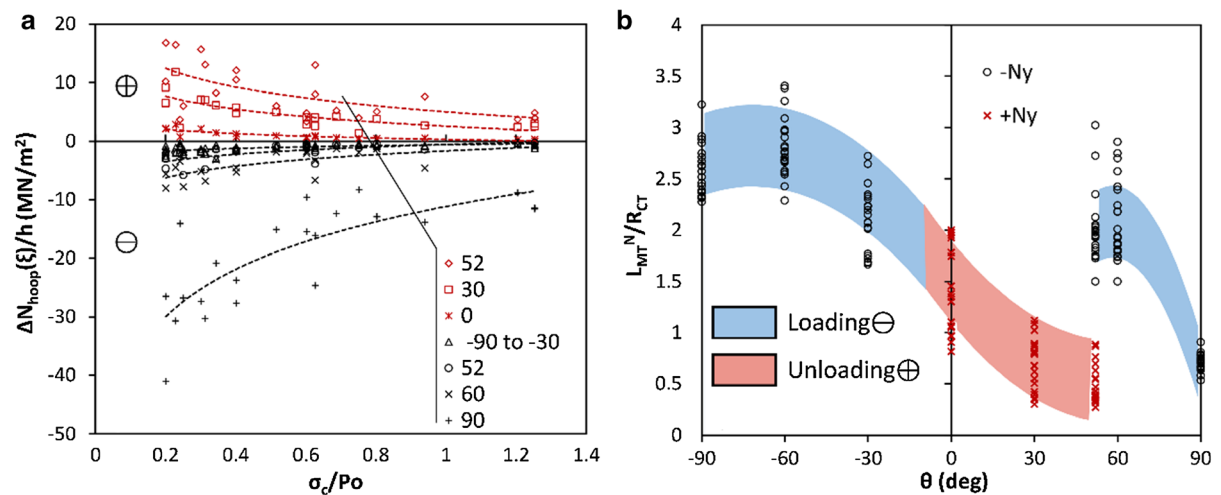
where  $x$  is the lateral distance from the centerline of the cross-tunnel (at  $x = 0$  in Fig. 3) and  $L_{MT}^N$  the width of the distribution. Values of  $\xi$  may be obtained from column 5 of Table 5. Values of  $\Delta N_{hoop}(\xi)$ , normalized with  $h$ , are plotted in Fig. 10a for various angles  $\theta$  (corresponding to the longitudinal profiles of

Fig. 3) with respect to  $\sigma_c/P_o$ . It is observed that for angles  $\theta = -90^\circ$  up to  $-30^\circ$  and approximately  $\theta = 60^\circ$  to  $90^\circ$  the main tunnel lining is loaded with additional compressive hoop axial forces. The most severely loaded area is found to be at the walls of the main tunnel (for  $\theta = 90^\circ$ ), while for the rest of the abovementioned angles, the additional compressive hoop axial forces are significantly lower. Contrary, for angles  $\theta$  from approximately  $0^\circ$  to  $52^\circ$  the additional hoop axial forces are tensile, indicating an unloading of this area, which may even result in tensile loading after excavation of the cross-tunnel.

Especially for  $\theta = 52^\circ$ , in the neighborhood of the junction area tensile additional hoop axial forces are observed indicating an unloading of the main tunnel lining there. However, the area away from the junction is loaded by additional compressive axial forces. In that section, the distribution of the additional hoop axial forces is described by a two branch equation, with one branch for the unloading area (applicable for  $|x| < R_{CT}$ ) and one branch for the loaded area (applicable for  $|x| > R_{CT}$ ). This is explained in Fig. 11.

$\Delta N_{hoop}(\xi)$  per unit length [MN/m] may be evaluated from the following equation:

$$\Delta N_{hoop}(\xi) = \left[ a_1 \ln\left(\frac{\sigma_c}{P_o}\right) + c_1 \right] h \tag{9}$$



**Fig. 10** **a** Change in normalized axial hoop forces after the construction of the escape tunnel for various degrees  $\theta$  and  $\sigma_c/P_o$  values, **b** normalized width of axial hoop forces after the construction of the escape tunnel for various angles  $\theta$

**Table 5** Average values required in Eqs. 8 and 9 for the estimations of additional hoop axial forces along each longitudinal profile

$\theta$ (°)	$\alpha_1$ [MN/m <sup>2</sup> ]	$c_1$ [MN/m <sup>2</sup> ]	$\xi$	$L_{MT}^N/R_{CT}$
<i>Loading</i>				
− 90	0.70	− 0.60	0	2.58
− 60	0.70	− 0.60	0	2.91
− 30	0.70	− 0.60	0	2.12
52 <sup>a</sup>	1.82	− 0.57	0	2.01
60	2.85	− 1.66	$\pm R_{CT}/2$	2.08
90	11.7	− 11.18	$\pm R_{CT}$	0.71
<i>Unloading</i>				
0	− 1.09	0.30	0	1.44
30	− 3.18	2.57	0	0.70
52 <sup>b</sup>	− 4.60	5.02	0	0.48

<sup>a</sup>For  $|x| > R_{CT}$

<sup>b</sup>For  $|x| \leq R_{CT}$

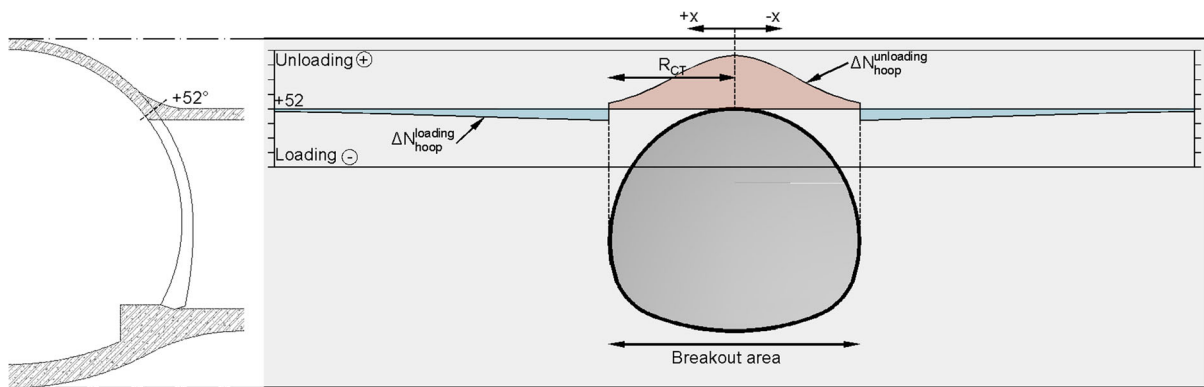


**Fig. 11** Schematic representation of the additional hoop axial forces distribution for  $\theta = 52^\circ$

where  $\alpha_1, c_1$  are constants with dimension of stress (MN/m<sup>2</sup>) that may be obtained from columns 3 and 4 of Table 5,  $\sigma_c$  the rock mass uniaxial compressive strength,  $P_0$  the in situ stress and  $h$  the thickness of the main tunnel lining.

The values of the width  $L_{MT}^N$  of the additional hoop axial forces distribution, normalized with the cross-tunnel crown radius  $R_{CT}$ , are presented in Fig. 10b. It is observed that the most affected area along the main tunnel lining varies from  $1.5 R_{CT}$  to  $3 R_{CT}$  except for  $\theta = 90^\circ$  where it is lower than  $R_{CT}$ . This implies that the severe maximum additional compressive loading there is acting only locally. For approximately  $\theta = 30^\circ$  to  $52^\circ$ , where the additional hoop axial forces are tensile,  $L_{MT}^N$  varies from  $0.5 R_{CT}$  to  $2 R_{CT}$ . For the most severe unloading location at  $\theta = 52^\circ$ ,  $L_{MT}$  varies from  $0.5 R_{CT}$  to  $1 R_{CT}$ . This implies that the severe maximum additional tensile unloading there is acting only locally.

In all cases loading (compression) is negative and unloading (tension) is positive.

### 4.3 Bending Action (Hoop Bending Moments)

The hoop bending moments along the lining of a sequentially excavated and supported tunnel in stages (top head—bench/invert) vary along each excavation and support cycle due to the sequential construction, on both top head and bench/invert. After the breakout and the sequential excavation and support of the escape tunnel, the hoop bending moments of the existing main tunnel lining are affected along the entire junction area. The absolute values of the additional hoop bending moments are presented in Fig. 12. The maximum value is observed at the floor of the main tunnel lining at the area of the junction due to the unloading of the rock mass there after excavation of the cross tunnel. This is partially a numerical error, since the constitutive model used does not take into

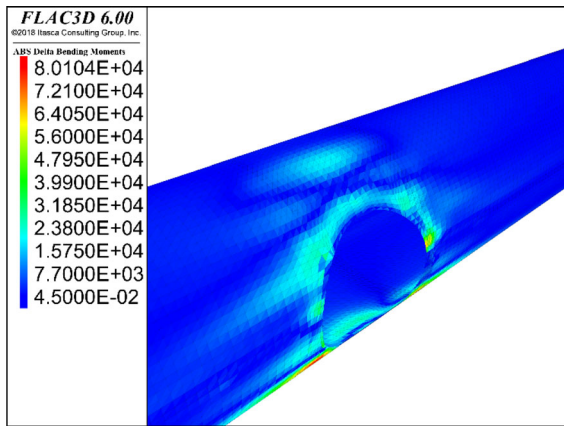


**Fig. 12** Absolute change of the hoop bending moments after the construction of the escape tunnel

account a higher Young’s modulus under unloading conditions, leading to unrealistic lifting of the tunnel floor after the removal of the cross-tunnel material. Those bending moments are developed to the already installed lining of the main tunnel, but do not affect the lining of the cross-tunnel that is loaded from the excavation of the following cross-tunnel stage. The cross-tunnel lining bending moments are generally lower at the junction area than the respective values away from the junction area.

The maximum absolute values of the hoop bending moments change  $\Delta M_{hoop}(\xi)$  [MNm/m] at the junction area, normalized by  $h^2$  of each support category A to D used in each numerical model, are presented in Fig. 13a for the various angles  $\theta$  ( $-90^\circ$  to  $+90^\circ$ ) corresponding to the longitudinal profiles of Fig. 3. It may be observed that the most affected area of the junction is located at the sidewall of the main tunnel lining. The hoop bending moments change becomes significant only for low values of the normalized rock mass strength  $\sigma_c/P_o$ .

The distribution of the hoop bending moments change along each longitudinal profile may be expressed with a Gaussian “bell curve” distribution with maximum value  $\Delta M_{hoop}(\xi)$  [MNm/m] acting at lateral distance  $x = \xi$ , and width  $L^M_{MT}$ :

$$\Delta M_{hoop}(x) = \Delta M_{hoop}(\xi) e^{-\frac{(x-\xi)^2}{2L^M_{MT}}} \tag{10}$$

Average values of  $\xi$  for each angle  $\theta$  may be obtained from column 4 of Table 6. The range of  $L^M_{MT}$  values, normalized with the cross-tunnel crown

radius  $R_{CT}$ , are presented in Fig. 13b while average  $L^M_{MT}$  values for each angle  $\theta$  may be obtained from column 5 of Table 6.

$\Delta M_{hoop}(\xi)$  [MNm/m] may be estimated for each angle  $\theta$  as:

$$\Delta M_{hoop}(\xi) = a_2 \left( \frac{\sigma_c}{P_o} \right)^{c_2} h^2 \tag{11}$$

where the coefficients  $a_2$  and  $c_2$  may be obtained from columns 2 and 3 of Table 6. Note that  $a_2$  is a stress coefficient with dimensions of MNm/m<sup>3</sup>.

#### 4.4 Effect of the Tunnel Depth and Rock Mass Quality

The extreme values of the examined quantities (additional displacements, axial forces and bending moment) are located in two critical positions of the main tunnel lining. The first position is in the junction with the cross-tunnel crown (Area A of Fig. 9). In the specific portion of the main tunnel lining ( $\theta = 52^\circ$ ,  $x = 0$ ), the maximum additional displacements and the maximum unloading of the hoop axial forces of the lining are located. Figure 14 presents the additional displacements ( $\Delta u$ ) at the specific critical position ( $\theta = 52^\circ$ ,  $x = 0$ ) of the main tunnel lining for various examined values of the in situ stress ( $P_o$ ) and the rock mass uniaxial compressive strength ( $\sigma_c$ ). The contour plot of Fig. 14 is based directly on the results of the three dimensional simulations. For a tunnel in a rock mass with  $\sigma_c = 4$  MPa and initial field stress  $P_o = 8$  MPa, the maximum additional displacements are of the order of  $\Delta u = 4$  mm. An increase of the rock mass uniaxial compressive strength by 50% to  $\sigma_c = 6$  MPa will result in maximum additional displacement of the order of  $\Delta u = 2.4$  mm. With a 50% reduction of the initial field stress value to  $P_o = 4$  MPa, the additional displacements introduced to the main tunnel lining are of the order of  $\Delta u = 1.7$  mm. Hence, the additional displacements are related more to a favorable modification (reduction) of the in situ stress than a favorable increase of the rock mass strength. For an 50% unfavorable modification of the same values,  $\Delta u = 7$  mm for a  $\sigma_c = 4$  MPa and  $P_o = 12$  MPa, while  $\Delta u = 7.5$  mm for  $\sigma_c = 2$  MPa and  $P_o = 8$  MPa. In that unfavorable case, the additional displacements are almost equally related to the rock mass uniaxial compressive strength and the in situ stress.



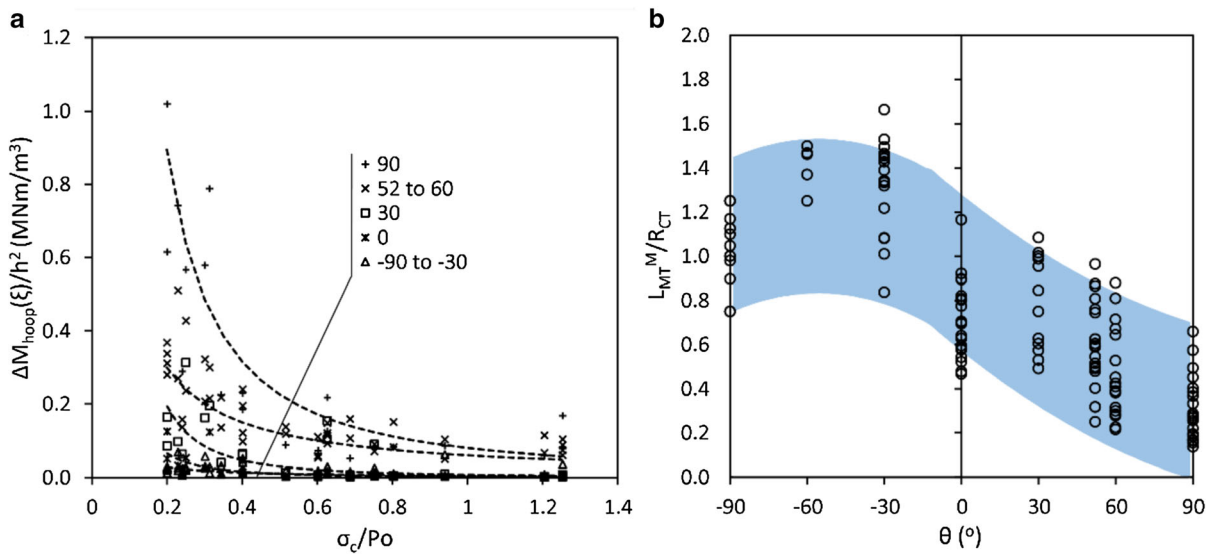


**Fig. 13** **a** Maximum change of normalized hoop bending moments after the construction of the escape tunnel with respect to the normalized rock mass strength for various angles  $\theta$ ,

**b** normalized width of hoop bending moments change distribution after the construction of the escape tunnel for various angles  $\theta$

**Table 6** Average values required in Eqs. 10 and 11 for the estimation of average hoop bending moments change along each longitudinal profile

$\theta$ (°)	$\alpha_2$ [MNm/m <sup>3</sup> ]	$c_2$	$\xi$	$L_{MT}^M/R_{CT}$
- 90	0.005	- 1.1	0	~ 1.04
- 60	0.005	- 1.1	0	~ 1.13
- 30	0.005	- 1.1	0	1.32
0	0.002	- 2.08	0	0.72
30	0.007	- 2.05	0	0.81
52	0.06	- 1.0	0	0.59
60	0.06	- 1.0	$\pm R_{CT}/2$	0.47
90	0.08	- 1.5	$\pm R_{CT}$	0.30

In the same critical portion ( $\theta = 52^\circ, x = 0$ ) of the main tunnel lining, the most severe unloading of the hoop axial forces is located. Figure 15 presents the maximum unloading of the hoop axial forces ( $+ \Delta N_{hoop}$ ) based on the three dimensional simulations at the specific critical position of the main tunnel lining for various examined values of the in situ stress ( $P_o$ ) and rock mass uniaxial compressive strength ( $\sigma_c$ ). The results follow the same pattern with the additional displacements contour of Fig. 14.

The second critical position of the main tunnel lining is in the junction with the cross tunnel side wall

(Area B of Fig. 9). In that portion of the main tunnel lining ( $\theta = 90^\circ, x = R_{CT}$ ), the maximum compressional loading of the hoop axial forces and bending moments are located. Figure 16 presents the effect of the rock mass uniaxial compressive strength ( $\sigma_c$ ) and of the in situ stress ( $P_o$ ) on the additional compressional loading introduced on the main tunnel side wall after the construction of the escape tunnel. For low quality rock masses, the compressional loading of the main tunnel lining is severe. In such cases, conservative excavation process and support system should be used in the intersection area.

Finally, Fig. 17 presents the absolute bending moments values introduced to the main tunnel lining after the construction of the cross tunnel. All the maximum values of the critical quantities with respect to the rock mass uniaxial compressive strength ( $\sigma_c$ ) and the in situ stress ( $P_o$ ) follow the same pattern.

The values of Figs. 14, 15, 16 and 17 may be used as a guideline to prevent the use of any unrealistic results from the proposed methodology due to its limitations.

### 5 Example Application and Validation of Results

As an example application of the proposed methodology for the evaluation of the loading conditions at

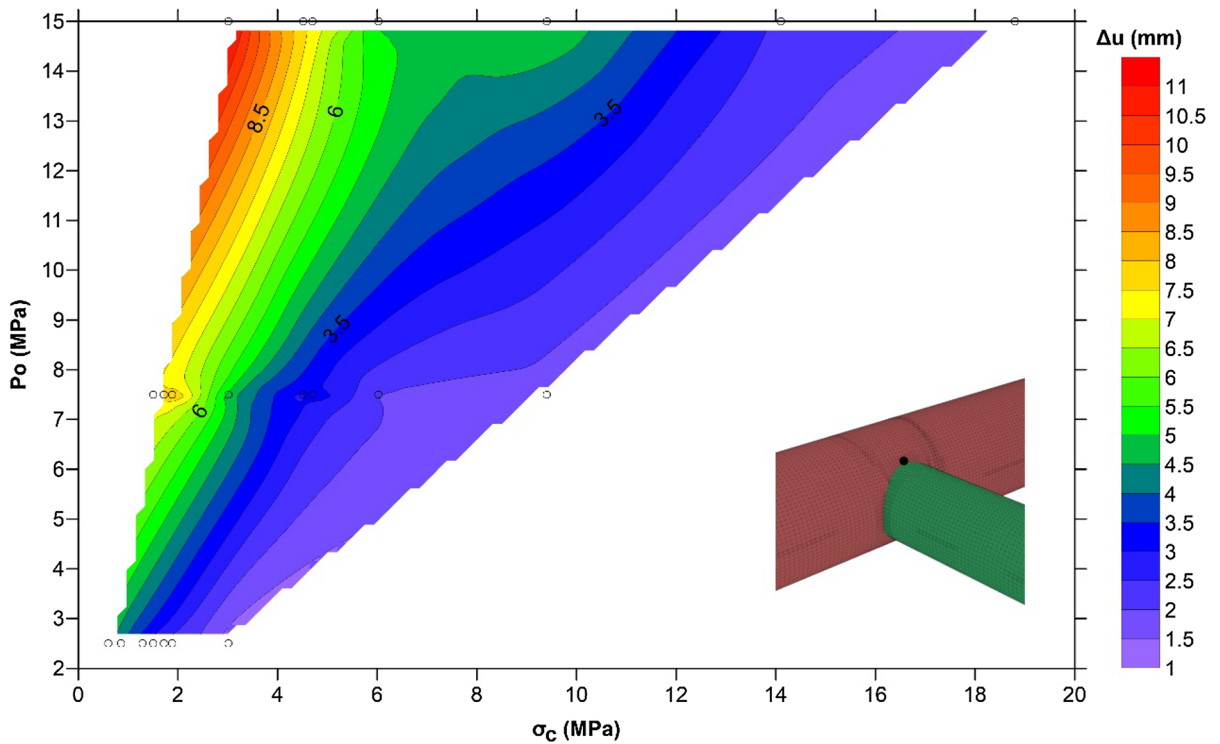


**Fig. 14** Maximum additional displacements of the main tunnel lining for various in situ stresses ( $P_o$ ) and rock mass uniaxial compressive strengths ( $\sigma_c$ ) at the junction area with the cross tunnel crown ( $\theta = 52^\circ, x = 0$ )

the junction area, the design case of a junction excavated in a rock mass with  $\sigma_c/P_o = 0.4$  is examined. The cross sections of both tunnels are presented in Fig. 1. Support classes B and AB of Table 1 were used for the main and cross tunnel respectively.

Plane strain simulations were carried out in order to estimate the displacements, the hoop axial forces  $N$  and the hoop bending moments  $M$  of the lining for the main and cross tunnel respectively, away from the junction area. The results of these simulations are presented in columns 3 through 5 of Table 7. Negative axial forces are compressive.

### 5.1 Estimation of Displacements at the Junction Area

The maximum additional displacements  $\Delta u_{MT}(\xi)$  induced to the lining of the main tunnel support, after the excavation of the cross tunnel, may be estimated e.g. from Fig. 5a or from Table 4, by using the value  $u_{CT}(\infty) = 0.27$  cm of the displacement at the crown of the cross tunnel away from the junction area, as obtained from the plane strain simulation. The

maximum additional displacements  $\Delta u_{MT}(\xi)$  are presented in column 6 of Table 7. Further, the distribution of the additional displacements along each longitudinal profile examined can be estimated from Eq. 6 by using the values of  $\xi$  and  $L_{MT}^u/R_{CT}$  for each angle  $\theta$  provided in Table 4. The results of this procedure are presented as a contour map on the unfolded view of the main tunnel lining shown in Fig. 18a.

The values along each longitudinal section can be summed to the displacements estimated from the plane strain model (Table 7) at the relevant angle to estimate the total displacements developed on the lining of the main tunnel after excavation of the cross tunnel.

The additional displacements evaluated from a three-dimensional numerical model in the examined case are presented as a contour map on the unfolded view of the main tunnel lining shown in Fig. 18b. By comparing Fig. 18a and b it may be observed that the additional displacements of both methods are in good agreement. The maximum additional displacement of the proposed method is of the order of 0.48 cm and of the three-dimensional model of the order of 0.46 cm.

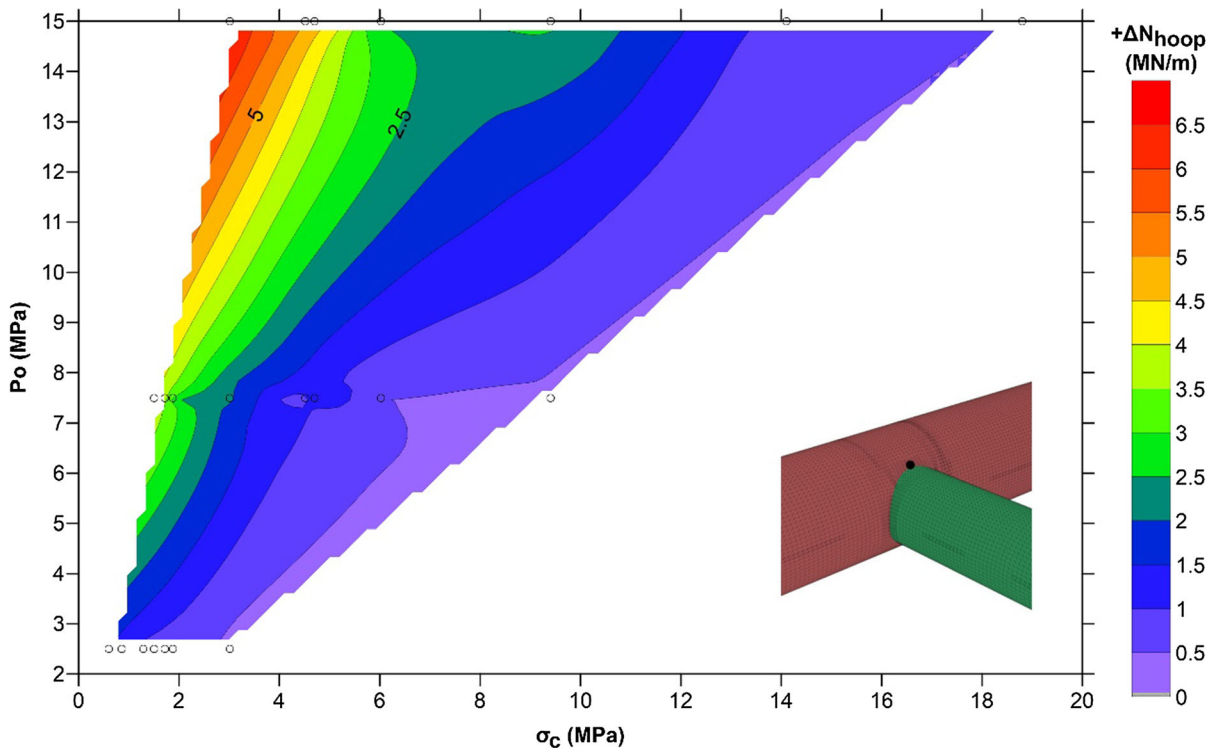


**Fig. 15** Maximum unloading of the main tunnel lining hoop axial forces ( $+ \Delta N_{hoop}$ ) for various in situ stresses ( $P_o$ ) and rock mass uniaxial compressive strengths ( $\sigma_c$ ) at the junction area with the cross tunnel crown ( $\theta = 52^\circ, x = 0$ )

The displacements calculated from the three-dimensional simulations along the crown of the cross tunnel where presented in Fig. 7. The maximum additional displacement  $\Delta u_{CT}(d)$  at the crown of the cross tunnel can be estimated from Fig. 8a as  $\Delta u_{CT}(d) = 0.13$  cm. The maximum total displacement  $u_{CT}(d)$  may be evaluated by adding the total displacement  $u_{CT}(\infty) = 0.27$  cm away from the junction area. A total displacement  $u_{CT}(d) = 0.40$  cm results. The cross tunnel crown displacements profile width  $L^u_{CT} = 8.8$  m may be obtained from Fig. 8b. Then, the cross tunnel crown displacements profile may be plotted by using Eq. 7 for  $y > d$ . The results of this procedure are presented in Fig. 7 and are in good agreement with the three-dimensional numerical results.

### 5.2 Axial Forces

The maximum change of the hoop axial forces  $\Delta N_{hoop}$  for each longitudinal profile (for the various angles  $\theta$  of Figs. 1 and 3) can be estimated either from Fig. 10b or from Eq. 9 with the coefficients  $\alpha_1$  and  $c_1$  of Table 5 and by considering the thickness of support class B

lining  $h = 0.2$  m. The  $\Delta N_{hoop}$  values obtained from this procedure are presented in column 7 of Table 7. The distribution of the hoop axial forces change along each longitudinal profile may be obtained from Eq. 8 for values of  $L^N_{MT}$  obtained from Table 5. The results of this procedure are presented as a contour map on the unfolded view of the main tunnel lining shown in Fig. 19a. Positive values indicate unloading and negative values compressive loading of the tunnel lining.

The change of the hoop axial forces evaluated from the three-dimensional model in the examined case are presented as a contour map on the unfolded view of the main tunnel lining shown in Fig. 19b. By comparing the contour maps of Fig. 19a and b it is observed that the change of the hoop axial forces values obtained from both methods are in good agreement. The maximum unloading at the unloading area A (Fig. 9) estimated by the proposed method is  $\Delta N_{hoop} = 1.84$  MN/m while that evaluated from the three-dimensional model is  $\Delta N_{hoop} = 2.1$  MN/m. The maximum additional compressive loading at loading area B (Fig. 9) estimated according to the proposed method

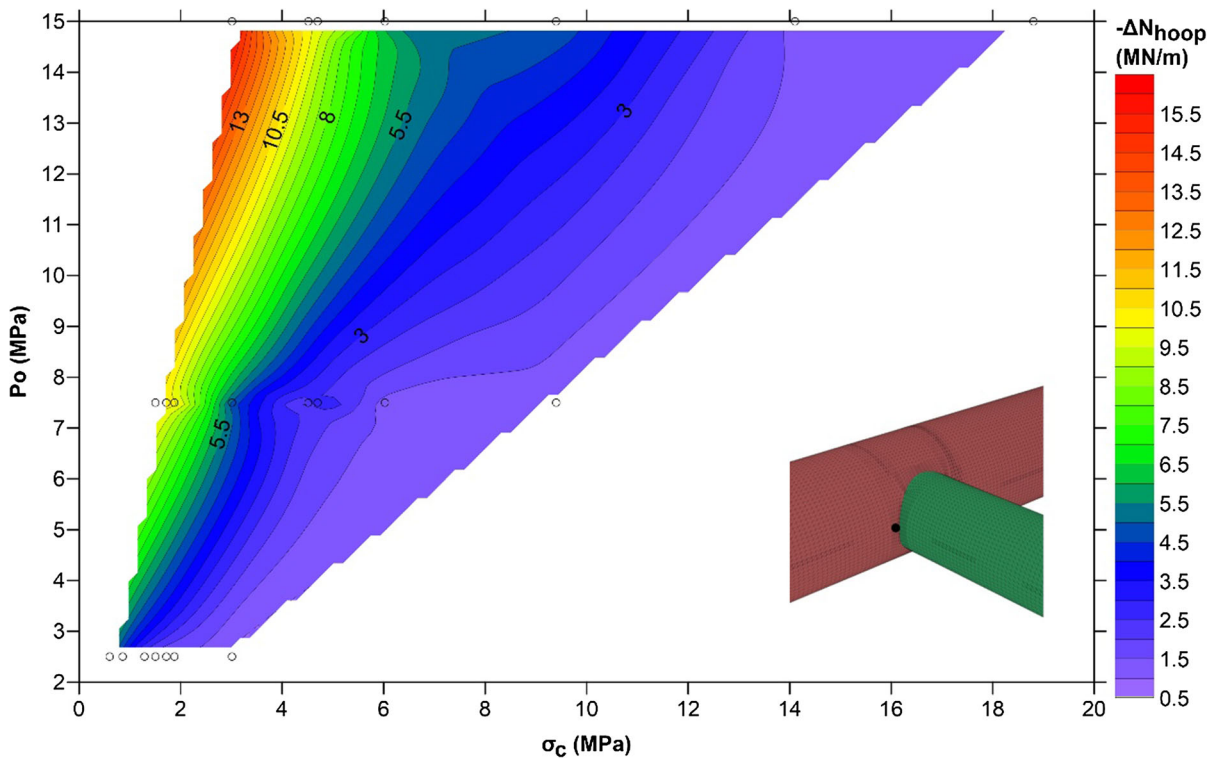


**Fig. 16** Maximum change of compressional hoop axial forces loading of the main tunnel lining ( $-\Delta N_{hoop}$ ) for various in situ stresses ( $P_o$ ) and rock mass uniaxial compressive strengths ( $\sigma_c$ ) at the junction area with the cross tunnel side wall ( $\theta = 90^\circ, x = R_{CT}$ )

is  $\Delta N_{hoop} = -4.3$  MN/m and that evaluated from the three-dimensional model is  $\Delta N_{hoop} = -5.4$  MN/m. It may be concluded that the proposed method is a good approximation of the three-dimensional simulation without however replacing the quality of it.

The change of the hoop axial forces values at the junction area estimated with the proposed method may be added to the hoop axial forces values before excavation of the escape tunnel to yield the total hoop axial forces. Hoop axial forces values before excavation of the escape tunnel may be accurately evaluated by a 3D analysis without excavation of the escape tunnel, as this would provide a more accurate estimation. However, in standard design practice plane strain simulations are commonly used for tunnel support dimensioning. Therefore, in this example the hoop axial forces values before construction of the escape tunnel are evaluated from plane strain simulations and may be obtained from column 4 of Table 7. These are presented in the contour map of Fig. 20a. The total hoop axial forces at the unloading area A (Fig. 9)

according to the proposed method is extensional and equal to  $N_{hoop} = 50$  kN/m and that of the three-dimensional model of the order of  $N_{hoop} = 500$  kN/m. The maximum compressive loading at the loading area B (Fig. 9) according to the proposed method is  $N_{hoop} = -5.3$  MN/m and that of the three-dimensional model of the order of  $N_{hoop} = -6.0$  MN/m.

The total hoop axial forces according to the three-dimensional numerical model are presented in Fig. 20b. In both the proposed method and the three-dimensional model the results indicate an area under tension at the main tunnel lining in the proximity to the crown of the cross tunnel and a compression area at the wall of the main tunnel at the junction area. The values obtained by the proposed method are in good agreement to the numerically obtained results by the 3D models, taking into account that the proposed method works with average values and does not take into account the variation of each value along every excavation step.

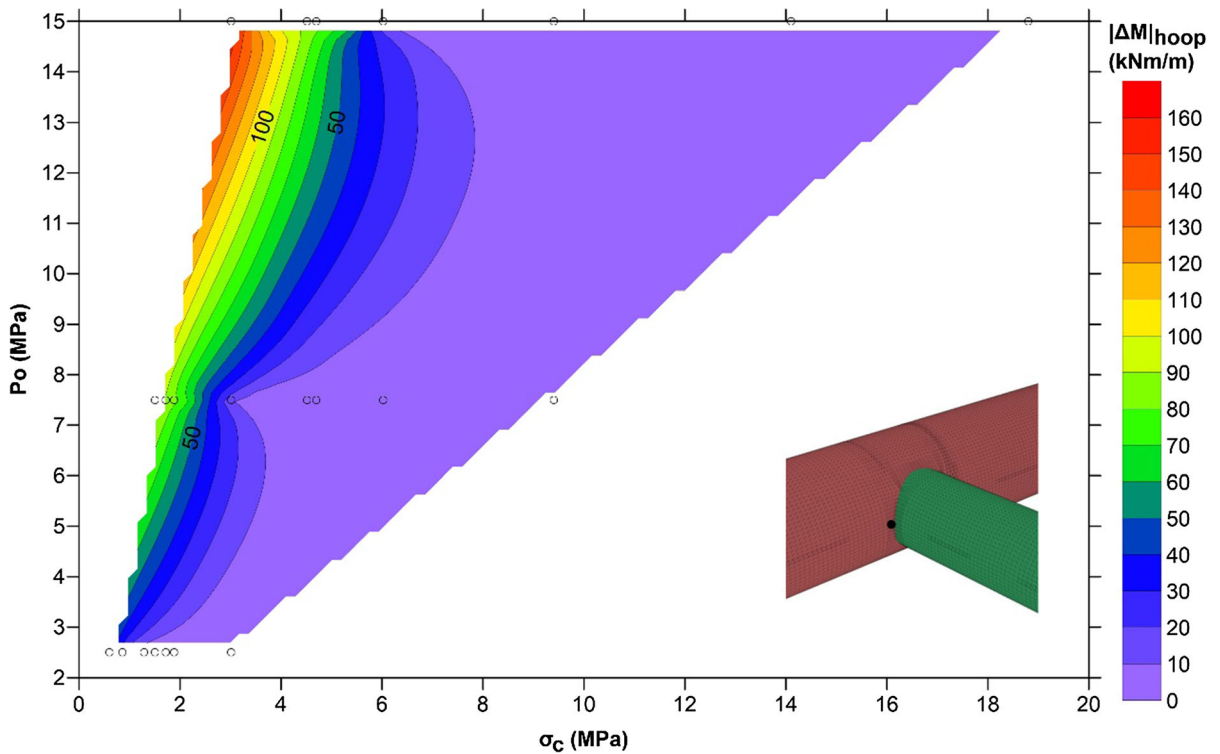


**Fig. 17** Maximum change of the absolute bending moments values of the main tunnel lining ( $|\Delta M|_{hoop}$ ) for various in situ stresses ( $P_o$ ) and rock mass uniaxial compressive strengths ( $\sigma_c$ ) at the junction area with the cross tunnel side wall ( $\theta = 90^\circ, x = R_{CT}$ )

**Table 7** Results of plane strain numerical simulations and proposed method maximum values

Main tunnel/cross tunnel	$\theta$ ( $^\circ$ )	Plane strain models			Proposed method		
		$u$ (cm)	$N$ (MN/m)	$ M $ (kNm/m)	$\Delta u(\xi)$ (cm)	$\Delta N_{hoop}(\xi)$ (MN/m)	$\Delta M_{hoop}(\xi)$ (kNm/m)
Main tunnel	- 90	0.48	- 1.04	3.84	$4.0 \times 10^{-3}$	- 0.24	0.51
	- 60	0.52	- 1.81	0.59	$3.9 \times 10^{-2}$	- 0.24	0.51
	- 30	0.46	- 1.61	2.70	$9.3 \times 10^{-2}$	- 0.24	0.51
	0	0.47	- 1.92	2.19	0.16	0.25	0.61
	30	0.46	- 1.59	2.67	0.27	1.09	1.8
	52	0.48	- 1.82	4.67	0.48	1.84/- 0.44	6.0
	60	0.52	- 1.6	2.05	0.43	- 0.85	6.0
	90	0.48	- 1	3.58	0.32	- 4.3	9.5
Cross tunnel	0	0.27	- 0.69	0.30	0.14	-	-

### 5.3 Bending Moments

The same methodology can be used for the estimation of the bending moments along the main tunnel lining. The maximum change of the hoop bending moments

$\Delta M_{hoop}$  for every longitudinal profile (Figs. 1, 3) can be estimated with Eq. 11 with the coefficients  $\alpha_2$  and  $c_2$  taken from Table 6. These values are shown in column 8 of Table 7. The distribution of the hoop bending moments change along each longitudinal



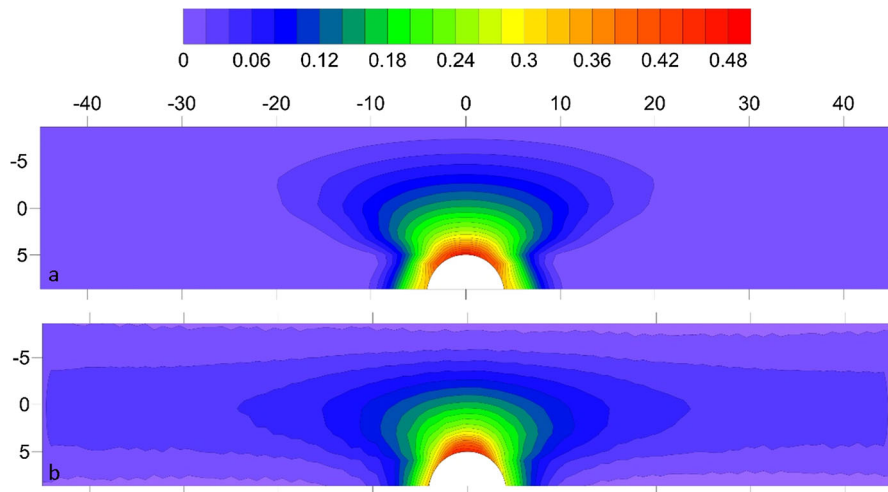


**Fig. 18** **a** Additional displacements (cm) on main tunnel lining after the construction of the escape tunnel estimated from Eq. 6 and Table 4, **b** additional displacements (cm) on main tunnel

lining after the construction of the escape tunnel evaluated from a 3D numerical simulation

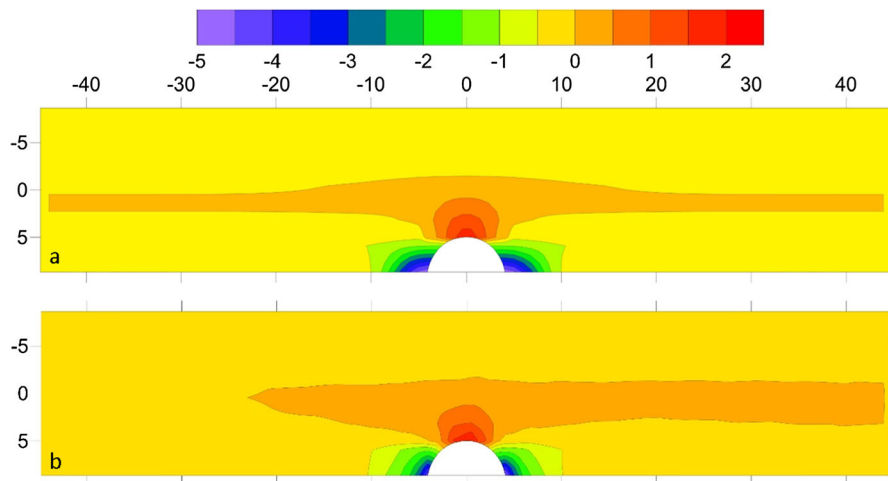


**Fig. 19** **a** Change of hoop axial forces (MN/m) estimated from Eqs. 8 and 9, **b** change of hoop axial forces (MN/m) from three dimensional simulations

profile may be found from Eq. 10 for  $L^M_{MT}$  obtained from Table 6 and by considering the thickness of support class B lining  $h = 0.2$  m. These values may be added to the hoop bending moment values obtained from the two-dimensional numerical simulation (column 5 in Table 7) to yield the total hoop bending moment values at the junction area. Similarly to the displacements and hoop axial forces, bending moments may be presented as contour maps on the unfolded view of the main tunnel lining.

#### 5.4 Dimensioning of the Main Tunnel Lining at the Junction Area

For the dimensioning of the main tunnel lining at the junction area, the total axial forces and bending moments are required. Figure 21a presents the M–N interaction diagram of the unreinforced section according to EC-2 for support class B used for the main tunnel and for a characteristic shotcrete strength  $f_{ck} = 25$  MPa. On the same plot, the axial forces and bending moments of the main tunnel, prior to the

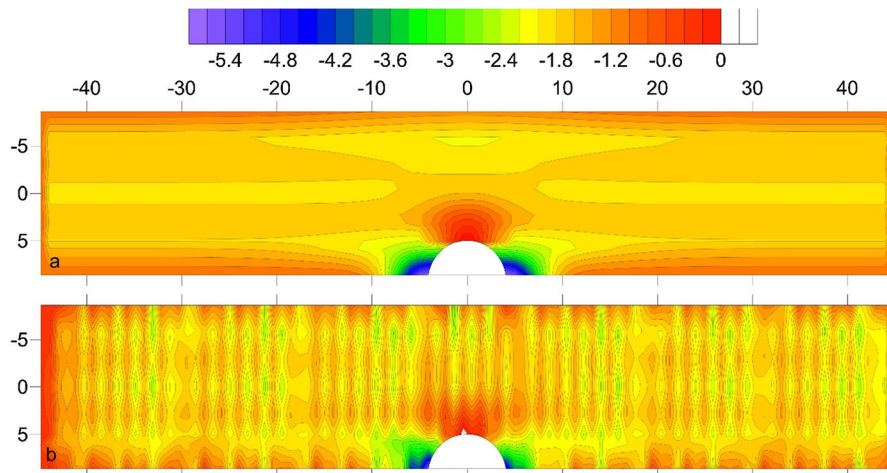


**Fig. 20** **a** Total hoop axial forces (MN/m) according to the proposed method, **b** total hoop axial forces (MN/m) according to the three dimensional simulations

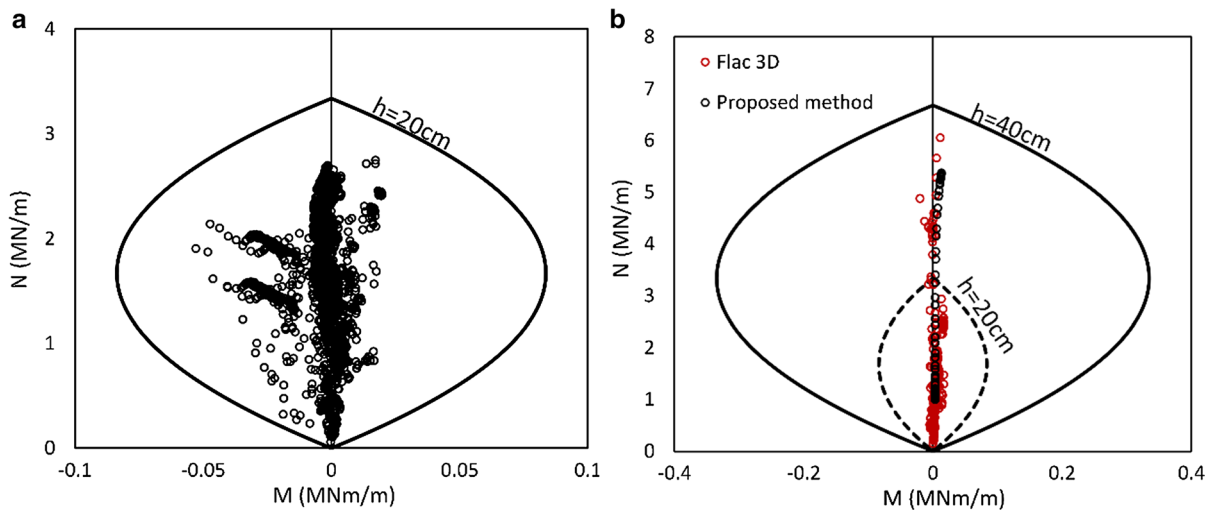


**Fig. 21** **a** M–N interaction diagram of support class B and lining axial forces and bending moments. **b** Axial forces and bending moments at the compression area ( $\theta = 60^\circ$  and  $90^\circ$ ) of the junction and interaction diagrams for  $h = 20$  and  $40$  cm

construction of the cross tunnel, as evaluated from the three dimensional simulation are presented. Since all the M–N points are within the capacity envelop, the lining can handle the internal forces developed from the construction of the main tunnel. After the construction of the cross tunnel, the junction area is unloaded in area A (Fig. 9) and loaded in area B. The results of the axial forces and bending moments in the compressional area B ( $\theta = 60^\circ$  and  $90^\circ$ ) from both the proposed method and the three-dimensional models are presented in Fig. 21b. Both methods estimate similar results. The additional loading at the examined

area is severe and the lining fails in compression. In the examined case the required thickness of the lining is of the order of 40 cm, twice its initial thickness.

As already discussed, in unloading area A the axial forces are tensional, hence reinforcement of the shotcrete is required.

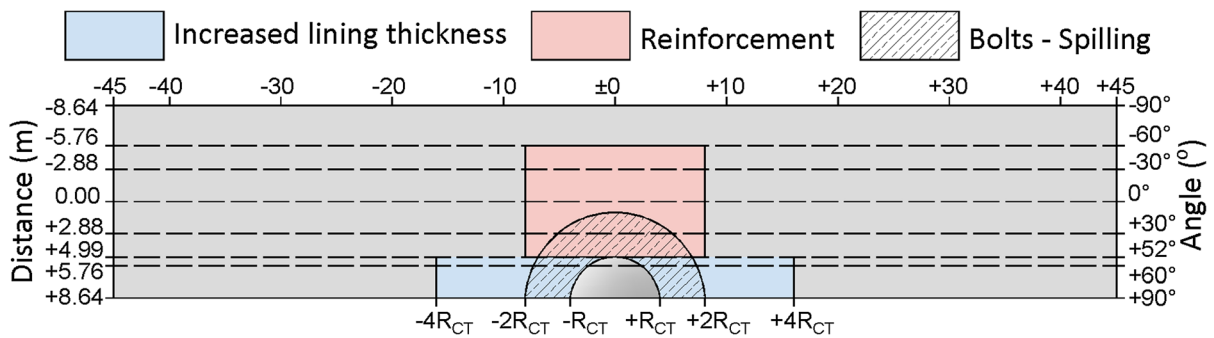


**Fig. 22** Schematic representation of the areas requires additional support

## 6 Conclusion

Based on the results of the three dimensional numerical simulations of the current study, the following conclusion are summarized:

- The results of this paper provide a practical way to take into account the effect of the cross tunnel to the main tunnel support system. It is essential that the main tunnel is constructed prior to the cross tunnel.
- The junction area of the main tunnel support with the cross tunnel crown is severely unloaded and tensional forces are likely to occur after the cross-tunnel construction. In that area, it is proposed to reinforce the main tunnel lining with e.g. the use of steel mesh and/or lattice girders to avoid tensional cracks in the shotcrete. The extensional area may expand up to two cross tunnel diameters ( $2R_{CT}$ ) along the main tunnel. The area that requires reinforcement is schematically presented in Fig. 22.
- The junction area of the main tunnel support with the cross tunnel side walls is loaded, and severe compressional forces are likely to occur. In that area, it is proposed to increase the lining thickness or to predict the construction of elephant foot to avoid compressional failure of the shotcrete. The compression area may expand up to four cross tunnel diameters ( $4R_{CT}$ ) along the main tunnel. The area that requires increased lining thickness or the construction of an elephant foot is schematically presented in Fig. 22.
- The axial forces and bending moments of the cross tunnel at the junction area are lower than those away from the junction area.

- Since the orientation of the excavation wall at the junction area is complex, wedge failure may occur in jointed rock masses, while instabilities may occur in very blocky rock masses. Hence, additional rock bolts, steel mesh and spilling may be required for failure control and according to rock mass jointing. The area that requires additional rock bolts, steel mesh and spilling is schematically presented in Fig. 22.
- It is generally proposed to use three dimensional simulations with sequentially excavated and supported tunnels, since tunnel junctions is a pure three-dimensional problem.
- The equations proposed should be used with caution to the limitations and in conjunction with and by considering the scattering of the results presented in the relevant figures and the maximum values presented in Figs. 14, 15, 16 and 17.

## References

- Alejano LR, Alonso E, Rodríguez-Dono A, Fernández-Manín G (2010) Application of the convergence-confinement method to tunnels in rock masses exhibiting Hoek–Brown strain-softening behaviour. *Int J Rock Mech Min Sci* 47:150–160. <https://doi.org/10.1016/j.ijrmm.2009.07.008>
- Alejano LR, Rodríguez-Dono A, Veiga M (2012) Plastic radii and longitudinal deformation profiles of tunnels excavated in strain-softening rock masses. *Tunn Undergr Space Technol* 30:169–182. <https://doi.org/10.1016/j.tust.2012.02.017>
- Bian K, Liu J, Xiao M, Liu Z (2016) Cause investigation and verification of lining cracking of bifurcation tunnel at Huizhou Pumped Storage Power Station. *Tunn Undergr Space Technol* 54:123–134. <https://doi.org/10.1016/j.tust.2015.10.030>

- Brown ET, Hocking G (1976) Use of the three dimensional boundary integral equation method for determining stresses at tunnel intersections. In: 2nd Australian tunnelling conference, Melbourne, pp 55–64
- Cai M, Kaiser PK, Tasaka Y, Minami M (2007) Determination of residual strength parameters of jointed rock masses using the GSI system. *Int J Rock Mech Min Sci* 44:247–265. <https://doi.org/10.1016/j.ijrmms.2006.07.005>
- Chen CN, Tseng CT (2010) 2D tunneling chart from redistributed 3D principal stress path. *Tunn Undergr Space Technol* 25:305–314. <https://doi.org/10.1016/j.tust.2010.01.003>
- Cundall PA, Carranza-Torres C, Hart RD (2003) A new constitutive model based on the Hoek-Brown criterion. In: Andrieux P, Brummer R, Detournay C, Hart R (eds) *FLAC and numerical modeling in geomechanics 2003*. Proceedings 3rd international FLAC symposium, Balkema, Lisse, pp 17–25
- Deere DU, Miller RP (1966) Engineering classification and index properties of rock. Technical report Air Force Weapons Lab., New Mexico, pp 65–116
- Gaspari GM, Zanoli O, Pescara M (2010) In Three-dimensional modelling of the tunnel intersections in weak rock mass on the kadikoy-kartal metro line of istanbul. In: *Rock mechanics civil and environmental engineering—proceedings of the European rock mechanics symposium EUROCK 2010*, pp 491–494
- Gerçek H (1986) Stability considerations for underground excavation intersections. *Min Sci Technol* 4:49–57. [https://doi.org/10.1016/S0167-9031\(86\)90194-5](https://doi.org/10.1016/S0167-9031(86)90194-5)
- Guan L, Baldauf SH, Chen WP (1994) Three dimensional simulation of progressive tunneling process for lining design of intersecting tunnels in soft rock. In: *Computing in civil engineering* (New York), pp 2006–2013
- Hocking G (1978) Stresses around tunnel intersections. In: *Computer methods in tunnel design*, pp 41–60. <https://doi.org/https://doi.org/10.1680/cmitd.00568.0003>
- Hoek E, Brown ET (2019) The Hoek–Brown failure criterion and GSI-2018 edition. *J Rock Mech Geotech Eng* 11:445–463. <https://doi.org/10.1016/j.jrmge.2018.08.001>
- Hoek E, Diederichs MS (2006) Empirical estimation of rock mass modulus. *Int J Rock Mech Min Sci* 43:203–215. <https://doi.org/10.1016/j.ijrmms.2005.06.005>
- Hoek E, Marinos P (2000) Predicting tunnel squeezing problems in weak heterogeneous rock masses. *Tunnels Tunn Int Part 1–2*:1–20
- Hoek E, Carranza C, Corkum B (2002) Hoek-Brown failure criterion-2002 edition. Narms-Tac. [https://doi.org/10.1016/0148-9062\(74\)91782-3](https://doi.org/10.1016/0148-9062(74)91782-3)
- Hsiao FY, Wang CL, Chern JC (2009) Numerical simulation of rock deformation for support design in tunnel intersection area. *Tunn Undergr Space Technol* 24:14–21. <https://doi.org/10.1016/j.tust.2008.01.003>
- Itasca Consulting Group Inc. (2017) *FLAC3D—fast Lagrangian analysis of continua in three-dimensions*, Ver. 6.0. Itasca, Minneapolis
- Jones B (2007) Stresses in sprayed concrete tunnel junctions. University of Southampton, Southampton. <https://doi.org/10.13140/RG.2.2.14046.84801>
- Li Y, Jin X, Lv Z, Dong J, Guo J (2016) Deformation and mechanical characteristics of tunnel lining in tunnel intersection between subway station tunnel and construction tunnel. *Tunn Undergr Space Technol* 56:22–33. <https://doi.org/10.1016/j.tust.2016.02.016>
- Lin P, Zhou Y, Liu H, Wang C (2013) Reinforcement design and stability analysis for large-span tailrace bifurcated tunnels with irregular geometry. *Tunn Undergr Space Technol* 38:189–204. <https://doi.org/10.1016/j.tust.2013.07.011>
- Liu X, Wang Y (2010) Three dimensional numerical analysis of underground bifurcated tunnel. *Geotech Geol Eng* 28:447–455. <https://doi.org/10.1007/s10706-010-9304-x>
- Marinos P, Marinos V, Hoek E (2007) Geological Strength Index (GSI). A characterization tool for assessing engineering properties for rock masses. In: Romana M, Peruchó Á, Olalla C (eds) *Underground works under special conditions*. Taylor & Francis, Boca Raton, pp 13–21. <https://doi.org/10.1201/noe0415450287.ch2>
- Spyridis P, Bergmeister K (2015) Analysis of lateral openings in tunnel linings. *Tunn Undergr Space Technol* 50:376–395. <https://doi.org/10.1016/j.tust.2015.08.005>

**Publisher's Note** Springer Nature remains neutral with regard to jurisdictional claims in published maps and institutional affiliations.